This is a repository copy of *Nonlocal hydrodynamic influence on the dynamic contact angle: Slip models versus experiment*.

White Rose Research Online URL for this paper:
http://eprints.whiterose.ac.uk/3652/

Article:

Published paper
Wilson, M. C. T., Summers, J. L., Shikhmurzaev, Y. D., Clarke, A. & Blake, T. D.
(2006) *Nonlocal hydrodynamic influence on the dynamic contact angle: Slip
models versus experiment,* Physical Review E , Volume 73 (4), 041606.

Non-local hydrodynamic influence on the dynamic contact angle: slip models vs experiment

Mark C. T. Wilson* and Jonathan L. Summers

School of Mechanical Engineering, University of Leeds, Leeds, LS2 9JT, UK

Yulii D. Shikhmurzaev†

School of Mathematics, University of Birmingham, Birmingham B15 2TT, U.K

Andrew Clarke

Kodak European Research, Cambridge CB4 0TP, U.K.

Terence D. Blake

Center for Research in Molecular Modeling, University of Mons-Hainaut, 20 Place du Parc, B–7000, Mons, Belgium

Experiments reported by Blake *et al.* [Phys. Fluids. **11**, 1995 (1999)] suggest that the dynamic contact angle formed between the free surface of a liquid and a moving solid boundary at a fixed contact-line speed depends on the flow field/geometry near the moving contact line. The present paper examines quantitatively whether or not it is possible to attribute this effect to bending of the free surface due to hydrodynamic stresses acting upon it and hence interpret the results in terms of the so-called "apparent" contact angle. It is shown that this is not the case. Numerical analysis of the problem demonstrates that, at the spatial resolution reported in the experiments, the variations of the "apparent" contact angle (defined in two different ways) caused by variations in the flow field, at a fixed contact-line speed, are too small to account for the observed effect. The results clearly indicate that the actual (macroscopic) dynamic contact angle, i.e. the one used in fluid mechanics as a boundary condition for the equation determining the free surface shape, must be regarded as dependent not only on the contact-line speed but also on the flow field/geometry in the vicinity of the moving contact line.

I. INTRODUCTION

Experiments reported by Blake *et al.* [1] pose a fundamental question for the mathematical modelling of dynamic wetting. The essence of the results is that at a fixed contact-line speed the dynamic contact angle — the angle at which the free surface meets the moving solid boundary — depends on the flow field/geometry in the vicinity of the moving three-phase-contact line. Specifically, it was demonstrated in curtain coating (Fig. 1), where a liquid sheet falls vertically onto a moving solid substrate, for a given gas/liquid/solid system and a given contact-line speed, the measured dynamic contact angle can be varied by varying the flow rate and/or the curtain height, that is the other parameters determining the flow field. A typical dependence of the measured dynamic contact angle on the flow rate for different contact-line speeds is given in Fig. 2. This result extended the one reported earlier [2], where critical conditions for the onset of air entrainment were found to be dependent on the flow field and a term 'hydrodynamic assist of dynamic wetting' was coined to describe this effect.

The onset of air entrainment is by no means an artifact of observations, and the effect of 'hydrodynamic assist' is used in applications of curtain coating, for example, in manufacturing photographic papers. However, the situation with the contact-angle behaviour in regular wetting is more subtle. A question which naturally arises is whether the observed effect of the contact-angle dependence on the flow field/geometry can be attributed to bending of the free surface due to the hydrodynamic stresses acting upon it, as suggested previously for a number of low-resolution measurements (see e.g. Ref. [3]). In the experiments by Blake *et al.* [1] the spatial resolution of the contact angle measurements was sufficiently high for the associated length scale to be small compared with the characteristic length scale of the flow field variations due to changes in the flow conditions, and because of that the authors had to question such an explanation.

The goal of the present work is to check this argument quantitatively, that is to try to describe the experimental data presented in Ref. [1], in particular those given in Fig. 2, within the framework of a conventional approach to the moving contact-line problem, which is based on (i) relaxing the no-slip boundary condition at the solid surface to remove the shear-stress singularity at the contact line and (ii) prescribing the actual contact angle to be a function of the contact-line speed and parameters characterizing the material properties of the contacting

---

*Electronic address: `m.wilson@leeds.ac.uk`
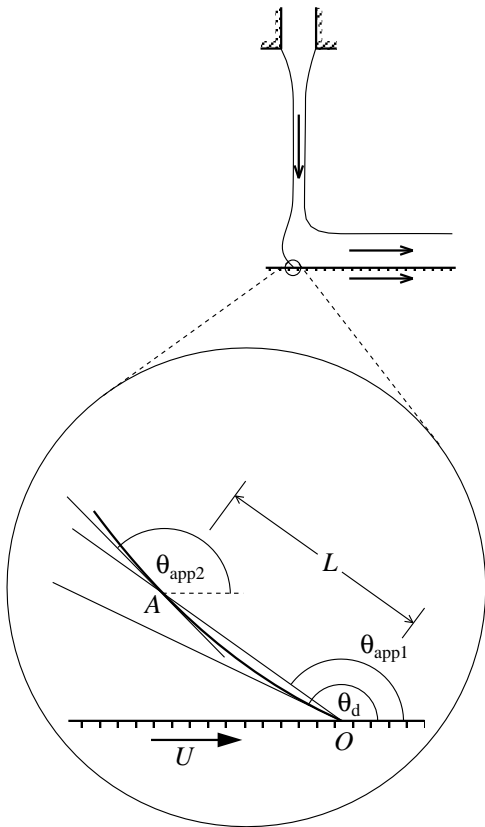†Electronic address: `yulii@for.mat.bham.ac.uk`

FIG. 1: A definition sketch for curtain coating. θ_d is the actual (macroscopic) contact angle, θ_{app1} and θ_{app2} are the "apparent" angles defined in different ways. In comparing continuum theories are with experiments, the length L becomes associated with the spatial resolution of the measurements.
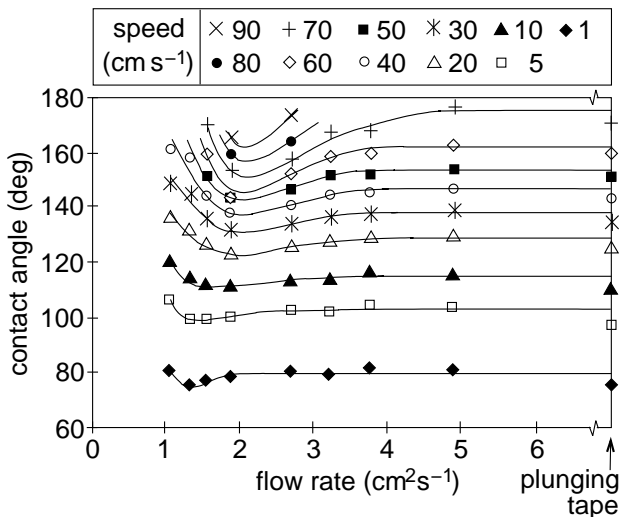

FIG. 2: Map of dynamic contact angle versus flow rate showing coating speed contours from Ref. [1] for curtain coating with a 3 cm high curtain of 25 mPas aqueous glycerol solution on PET tape. The spatial resolution of the measurements was less than 20 μm for all curves.

media. The models that use this approach are known collectively as 'slip models'.

In the experiments we will be trying to describe, the capillary and Reynolds numbers are of $O(1)$ so that we will have to consider slip models without any simplifications. Our objective is to find numerical solutions to the mathematical problem describing curtain coating in the framework of different slip models with all conditions and parameters coinciding with what was measured in experiments and to use free parameters of the models (such as the slip length) together with the actual contact angle θ_d (see Fig. 1) as adjustable, trying to fit the theory to the experiments.

II.   PROBLEM FORMULATION

To model the spreading of a Newtonian liquid over a solid surface, one has to overcome the well-known 'moving contact-line problem'. Mathematically, this comprises the following two components:

(i) The problem of removing the stress singularity at the moving contact line by formulating appropriate boundary conditions on the interfaces, instead of the classical ones, to account for the specific physics of the liquid-fluid displacement;

(ii) The problem of describing the dependence of the dynamic contact angle θ_d (Fig. 1), which is a boundary condition for the equation determining the free-surface shape, on the material properties of the contacting media, the contact-line speed and, possibly, other factors affecting the flow field.

These two aspects of the moving contact-line problem have been addressed in a number of works in the past three decades (see Sec. 9 in Ref. [4] for a review). The conventional approach to problem (i) is to preserve the classical boundary conditions on the free surface and relax no-slip on the solid boundary. In the literature, one can find two ways of imposing slip as a boundary condition at the solid surface. The first is to prescribe explicitly the velocity distribution near the moving contact line in the form

$$u = F(x; U, s_1, s_2, \ldots), \qquad (1)$$

where u is the tangential velocity of the liquid on the solid surface in the coordinate frame moving with the contact line, U is the (tangential) velocity of the solid in the same coordinate frame, x is the distance from the contact line, and s_i ($i = 1, 2, \ldots$) are constants specific to the gas/liquid/solid system. To remove the singularity at the contact line and satisfy the no-slip condition far away from it, one must have $F(0; \ldots) = 0$ and $F(x; \ldots) \to U$ as $x \to \infty$. Particular forms of (1) known in the literature are the exponential distribution [5–7]

$$u = U[1 - \exp(-\frac{x}{s_1})] \qquad (2)$$

and the algebraical ones [8]

$$u = U \frac{\left(\dfrac{x}{s_1}\right)^{s_2}}{1 + \left(\dfrac{x}{s_1}\right)^{s_2}}, \qquad s_2 = \tfrac{1}{2}, 1, 2. \qquad (3)$$

It is worth pointing out, however, that the general condition (1) and its particular forms (2), (3) are motivated more by their mathematical convenience than by physical arguments.

The second way of removing the stress singularity is to replace no-slip by the Navier condition [9], which assumes the slip velocity on the solid surface to be proportional to the tangential stress acting between liquid and solid:

$$\mu \frac{\partial u}{\partial y} = \beta (u - U). \qquad (4)$$

Here μ is the viscosity of the liquid; u and U are, as before, the tangential components of the velocities of the liquid and the solid surface, respectively, in a Cartesian coordinate frame moving with the contact line; y is the Cartesian coordinate normal to the solid surface; and β is the so-called 'coefficient of sliding friction' [10]. Particular expressions for β depend on the physical mechanisms assumed to be responsible for slip in the vicinity of the contact line, and are different for different models.

The conventional way of resolving problem (ii), common to all works in the area apart from that described in Ref. [11], is to assume that the actual dynamic contact angle θ_d (Fig. 1) is a function of the contact-line speed with respect to the solid surface, U, and a number of constants χ_i $(i = 1, 2, \ldots)$, which characterize the material properties of the contacting media:

$$\theta_d = f(U, \chi_1, \chi_2, \chi_3, \ldots). \qquad (5)$$

The parameters χ_i $(i = 1, 2, \ldots)$ may include the static contact angle θ_s, the known physical characteristics of the liquid and the liquid-gas interface, such as μ and the surface tension σ, some 'specific' material constants proposed to reflect the specific physics of the liquid-gas displacement, as well as empirical constants. In particular, if f is assumed to be independent of U, then θ_d becomes a 'material property' of the gas/liquid/solid system, and Eq. (5) turns into $\theta_d \equiv \theta_s$. This assumption has been made in a number of works and its validity is discussed in Sec. IV. The functional form of Eq. (5) also includes all empirical correlations (or 'master curves') proposed by different authors and reviewed by Hayes and Ralston [12].

The Navier-Stokes equations in the bulk together with the classical boundary conditions on the free surface, conditions (1) or (4) at the solid boundary, and a particular form of Eq. (5) to specify the dynamic contact angle, provide a well-posed mathematical problem, which is conventionally used to model coating flows. We will examine this approach to find out whether or not it allows one to describe the data given in Fig. 2.

It is necessary to emphasize that a number of so-called 'asymptotic models' advanced and intensively studied in the last decade all have the above formulation at their core. They concentrate on how one can obtain approximate results in the situation where some parameters (usually the capillary and Reynolds numbers) are asymptotically small. Our goal is to test the conventional approach itself by considering the corresponding models without any simplifications resulting from any approximate (asymptotic) treatment of the problem and use precisely the same (finite) values of all parameters as in the experiments of Blake *et al.* [1].

III. CONTACT ANGLE

One can see immediately that for a given gas/liquid/solid system and a given contact-line speed, all the arguments on the right-hand side of Eq. (5) become fixed, so that $\theta_d \equiv$ const independently of the flow field near the contact line. This conclusion is clearly in conflict with the results of Blake *et al.* [1], in particular with the data in Fig. 2, and we will examine whether one can get round this contradiction by considering hydrodynamic effects. The idea, which goes back to the early seventies [3], is to account for the fact that in experiments the spatial resolution in determining the free-surface location is always finite, so that within the length scale corresponding to this resolution the free surface can bend under the action of hydrodynamic stresses, thus leading to the deviation of the *measured* contact angle from θ_d. This idea resulted in the concept of the so-called "apparent" contact angle, an *ad hoc* quantity used to describe or interpret the experimental results. If in experiments the contact angle is extracted by indirect measurements [13, 14], then the spatial resolution of the measurements is in fact an extra unknown which, being scaled with the slip length, becomes an adjustable parameter used in fitting the theory to the data [15–17].

In the case of the data given in Fig. 2, the contact angle has been measured directly and the accuracy of measurements was known (less than $20 \, \mu$m for all curves), so that we can test the very idea of the apparent contact angle against the experiments.

First, we have to consider what is seen and measured in experiments and how the finite resolution of the measurements could be accounted for in a theoretical model. In experiments, the locations of both interfaces, the free surface and the solid boundary, are determined imprecisely so that effectively the interfaces are seen as 'layers' of a finite thickness rather than geometrical surfaces. The location of the contact line is determined with the same accuracy, and instead of the 'contact line' one can see a region where the above-mentioned layers overlap. It is the thickness of the layers representing the interfaces which is referred to as the nominal 'resolution' of the measurements. The contact angle is determined by fitting approximat-

ing curves to the experimentally observed shapes of interfaces (typically by eye or by computer assisted image processing) and then measuring the angle between the tangents to these approximating curves at the point of their intersection. Thus, the procedure implicitly involves averaging and extrapolation which are likely to increase considerably the accuracy of the contact-angle measurements, making the 'effective' resolution significantly higher (and hence the associated length scale considerably smaller) than the nominal one. However, in what follows we will neglect this effect and use the nominal resolution as the characteristic length scale associated with the measurements, since our approach is to interpret everything *in favour* of the idea of the apparent contact angle. It is clear that the free surface can bend more within a larger length scale corresponding to the 'nominal' resolution than within a much smaller 'effective' one.

Now, when we have an extra length scale, i.e. one associated with the accuracy of measurements, we can define the apparent contact angle in a theoretical (macroscopic) model, where, of course, the interfaces are described as geometrical surfaces of zero thickness and their locations are known precisely. For a given length scale L associated with the finite spatial resolution of the measurements (OA, Fig. 1) one can define the apparent contact angles in the theoretical model in the following two ways. First, it could be the angle between the solid surface and a chord connecting the contact line and a point on the free surface at distance L from the contact line, θ_{app1} (Fig. 1). This definition reflects the idea that in experiments we always deal with chords rather than tangents, and the resolution is simply the length of the corresponding chord. The second way to define the apparent contact angle is to consider the angle between the solid surface and the tangent to the free surface drawn at distance L from the contact line, θ_{app2} (Fig. 1). This definition is supposed to account for the difficulties in approaching the contact line experimentally. Just this definition has been used in a number of theoretical works [15, 16, 18]. Obviously, both θ_{app1} and θ_{app2} tend to θ_d as the accuracy of the contact-angle measurements increases. For sufficiently high resolutions, θ_{app1} is always between θ_{app2} and θ_d so that, strictly speaking, we could consider θ_{app2} only. However, we will look at the behaviour of θ_{app1} as well since it is θ_{app1} that mimics the experimental procedure of determining the contact angle [1]. The question we will try to answer in the following section is whether for the given spatial resolution the variation of θ_{app1} or θ_{app2} with flow rate is sufficient to account for the observed effect.

IV. METHODOLOGY

The procedure of comparing the numerical solutions obtained in the framework of the models sketched in Sec. II with the data given in Fig. 2 is as follows. First, we choose one of the conditions (2), (3) or (4) to remove the stress singularity and set its parameters. Those parameters are supposed to be material constants and hence independent of the flow rate. Then we choose the definition of the apparent contact angle, θ_{app1} or θ_{app2}; the spatial resolution OA (Fig. 1) is known from the experiments (for the data given in Fig. 2 a conservative estimate for the spatial resolution gives $L = 20$ μm). After that we can specify the value of θ_d, which, according to Eq. (5), must be independent of the flow rate as well. We will set the value of θ_d to make the chosen apparent contact angle equal to the measured one at *one* point of the angle-versus-flow rate experimental curve (Fig. 2). It is convenient to choose a point corresponding to a high flow rate, where the experimentally measured contact angle approaches the one measured in the standard plunging-tape experiment for the same contact-line speed [1]. Now, all the parameters of the model are set and we can vary the flow rate and follow the evolution of the theoretically calculated apparent contact angle. This will give us a theoretical curve to compare with the corresponding experimental one from Fig. 2. Then the procedure can be repeated for other values of parameters in the slip model, for another slip model, and for the other way of defining the apparent contact angle. We emphasize that for a given model after setting the values of all parameters in the way described above we vary only the flow rate while keeping the contact-line speed fixed.

The above-described procedure has been carried out using a numerical code based on the finite-element method. The essential numerical details are given in the Appendix.

V. RESULTS

The results of the calculations are shown in Figs. 3–6, where we compare theoretical curves with the experimental data from Fig. 2 corresponding to $U = 70$ cm s^{-1}.

For these results, the capillary number $Ca \equiv \mu U / \sigma = 0.273$ and the Reynolds number, $Re \equiv Q/\nu$, varies from 7.11 to 23.7 (here σ is the surface tension, ν the kinematic viscosity, and Q the flow rate). The values of θ_d prescribed in each case for the apparent contact angle to match the experimental one at high flow rates are given in Tables I and II for the slip models (2) and (4), respectively. Comparison with the other experimental curves from Fig. 2 gives results similar to those shown in Figs. 3–6.

As is clear from the figures, in all cases the changes in the apparent contact angle are too small to account for the experimentally observed effect of the flow field variation on the contact angle. The discrepancy cannot be attributed to experimental errors given that, as reported in Ref. [1], even in a single measurement the typical accuracy of determining the contact angle was about $\pm 5°$, whereas the data in Fig. 2 obtained after averaging over multiple measurements was significantly less than that.

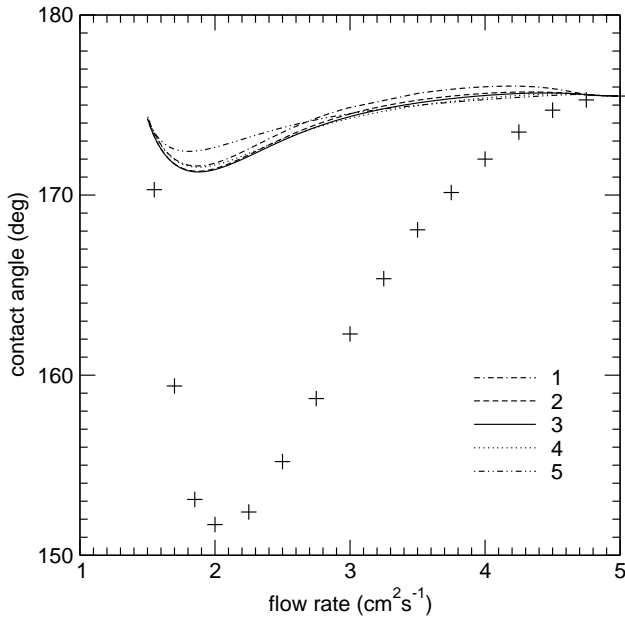Boundary conditions (3) lead to results similar to those

FIG. 3: Variation of θ_{app1} with flow rate for the model using a prescribed (exponential) slip-velocity distribution (2) with various slip lengths. Curves 1, 2, 3, 4 and 5 correspond to $s_1 = 0.01$, 0.1, 1, 10, 100 μm, respectively. The experimental data (+ + +) are taken from Fig. 2, $U = 70$ cm s^{-1}.

FIG. 4: Variation of θ_{app1} with flow rate for the model using the Navier condition (4) with various coefficients of sliding friction. Curves 1, 2, 3, 4 and 5 correspond to $\beta = 1000$, 100, 10, 1, 0.1 kg/(cm^2 s), respectively. The experimental data (+ + +) are taken from Fig. 2, $U = 70$ cm s^{-1}.

TABLE I: The values of θ_d required to match the "apparent" contact angles, θ_{app1} and θ_{app2}, to the experimentally measured contact angle (175.5°, flow rate: 5 cm^{2}s^{-1}) for a slip model with the exponential velocity distribution (2) and various slip lengths, s_1.

s_1 (μm)	θ_d for θ_{app1}	θ_d for θ_{app2}
0.01	166.80	169.18
0.1	170.55	172.15
1.0	173.25	174.15
10.0	174.93	175.37
100.0	175.81	176.31

TABLE II: The values of θ_d required to match the "apparent" contact angles, θ_{app1} and θ_{app2}, to the experimentally measured contact angle (175.5°, flow rate: 5 cm^{2}s^{-1}) for a slip model with the Navier condition (4) with various values of the coefficient of sliding friction, β.

β (kg cm^{-2} s^{-1})	θ_d for θ_{app1}	θ_d for θ_{app2}
1000.0	165.33	167.90
100.0	167.03	169.30
10.0	168.98	170.77
1.0	170.95	172.24
0.1	173.05	173.92

given in Figs. 3–6. One can also see from Figs. 3–6 that in all cases the magnitude of the apparent contact angle variation saturates as the slip length decreases, and the theoretical curves become practically undistinguishable from one another at smaller slip lengths. Further reduction of the slip length reverses the trend and the curves become more shallow. Thus, for a given distance OA (Fig. 1), which corresponds to the (known) spatial resolution of the measurements [1], in the whole range of slip lengths, s_1, or the values of the coefficient of sliding friction, β, neither "apparent" contact angle describes the behaviour of the experimental data. It should be noted that there are no more parameters in the slip models which would allow one to improve the fit.

The same conclusions also follow from an attempt to fit a theoretical curve to the data using the resolution (the distance OA, Fig. 1) as an *adjustable* parameter. Our calculations show that to make the "apparent" contact
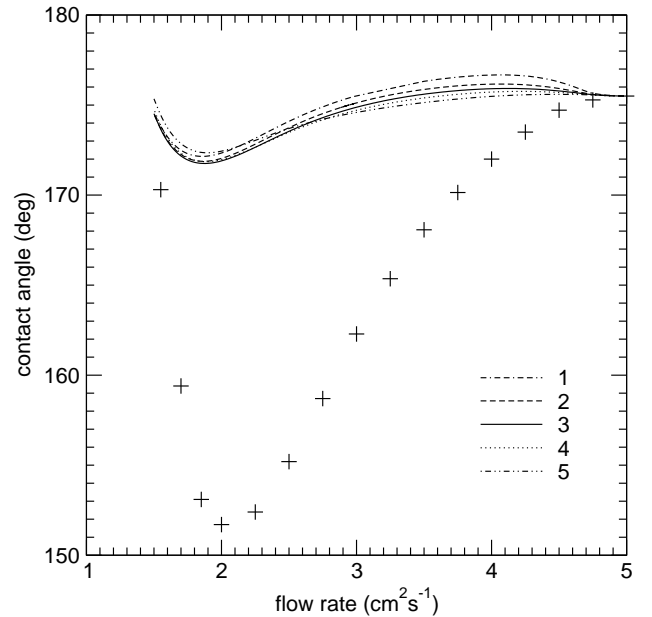
angle variation close to that of the observed contact angle the resolution has to be about 150 μm, i.e. about half the curtain thickness. This requirement is clearly beyond any reasonable interpretation of the measurements, as one can conclude simply by looking at the photograph of the curtain coating experiment, Fig. 4 in Ref. [1].

Thus, the simple arguments based on the order-of-magnitude analysis advanced by Blake *et al.* [1] are confirmed quantitatively, and one can assert that the influence of the flow field/geometry on the dynamic contact angle cannot be attributed entirely to bending of the free surface under the changing hydrodynamic stresses. At a fixed contact-line speed, the flow field variations caused by other factors do affect the *actual* contact angle.

This has serious implications for modelling. Indeed, the flow field is described by a set of partial differential equations whose solutions are fully determined by the boundary conditions formulated on all interfaces, in
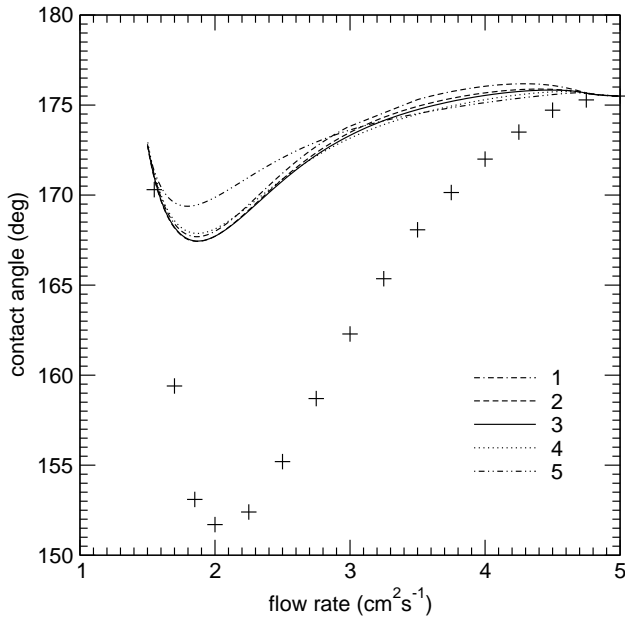
FIG. 5: Variation of θ_{app2} with flow rate for the model using a prescribed (exponential) slip-velocity distribution (2) with various slip lengths. Curves 1, 2, 3, 4 and 5 correspond to $s_1 = 0.01$, 0.1, 1, 10, 100 μm, respectively. The experimental data $(+ + +)$ are taken from Fig. 2, $U = 70$ cm s^{-1}.
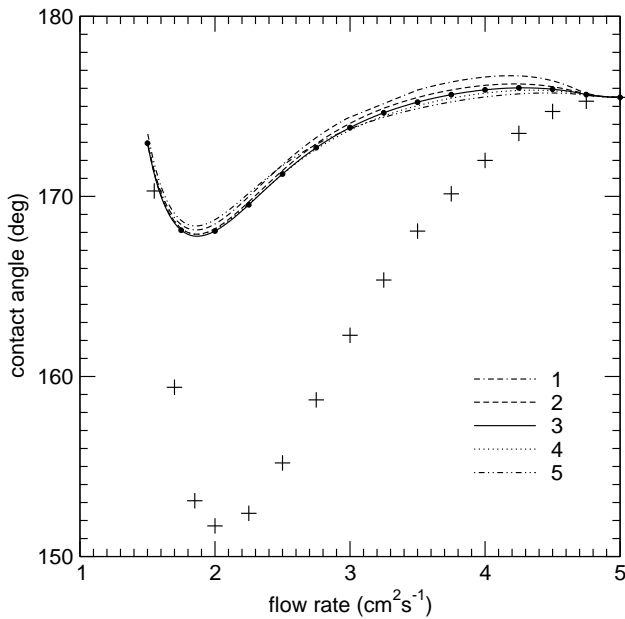

FIG. 6: Variation of θ_{app2} with flow rate for the model using the Navier condition (4) with various coefficients of sliding friction. Curves 1, 2, 3, 4 and 5 correspond to $\beta = 1000$, 100, 10, 1, 0.1 kg/(cm^2 s), respectively. The experimental data $(+ + +)$ are taken from Fig. 2, $U = 70$ cm s^{-1}. The black circles are data obtained in a repetition of the curve 3 calculation made using a mesh approximately twice as dense as the original.

other words, by a *continuous* set of data. Therefore, the description of the flow field cannot in principle be reduced to a *finite* (or even *countably* infinite) number of hydrodynamic factors, which could be put as arguments on the right-hand side of Eq. (5). Thus, the very functional form of Eq. (5) appears to be inadequate for modelling flows associated with moving contact lines in a general flow geometry. For a given liquid-solid system, the contact angle is not merely a function of the contact-line speed (and a number of other hydrodynamic factors); it is a *functional* of the flow field. In other words, the contact angle θ_d must be part of the solution. We will briefly discuss this issue in the next section.

A conclusion to be drawn from the tables is that in all cases θ_d is far from the static contact angle, θ_s: in the experiments $\theta_s = 67°$. Thus, our results do not support the assumption that $\theta_d \equiv \theta_s$ when the contact line is moving, which is used in a number of works [8, 16, 18–23]. This assumption needed the *ad hoc* concept of an "apparent" contact angle to describe the behaviour of the experimentally observed contact angle with the ratio of the resolution to the slip length as an adjustable parameter to fit the theory to the data. This approach was widely used for almost two decades, but gradually it became clear [5, 17] that even in treating the velocity dependence of the observed contact angle in standard pipe-flow experiments the assumption that $\theta_d \equiv \theta_s$ must be abandoned. The experiments of Blake *et al.* [1] and our calculations in the present paper provide a more general understanding of the reasons for that. Indeed, it was shown that θ_d depends on the flow field and, since the contact-line speed is the main factor influencing the flow field near the moving contact line, it will make θ_d deviate from θ_s even for what are, in other respects, similar flow conditions.

VI.   CONCLUSIONS

Our results show the following:

1). Bending of the free surface in the vicinity of the contact line and the resulting deviation of the so-called "apparent" contact angle from the actual one do not describe the effect observed in the experiments [1].

2). Therefore one has to conclude that, for a fixed contact-line speed, variations of the flow field in the vicinity of the moving contact line caused, for example, by other closely located boundaries do influence the *actual* dynamic contact angle, that is the angle which has to be used as a boundary condition in the fluid dynamical modelling of dynamic wetting. This effect cannot be described in the framework of the conventional approach to the moving contact line problem summarized in Sec. II.

3). The actual dynamic contact angle is equal neither

to the static (equilibrium) contact angle θ_s, as suggested, for example, in [22], nor, as is sometimes assumed [24, 25], to $180°$.

Thus, it has been shown that the conventional approach to the moving contact-line problem, which uses the functional form of Eq. (5) to determine the actual contact angle, is irreparably flawed and a different one is required.

At present, the only known theory that makes θ_d part of the solution and hence dependent on the bulk flow is the one developed in [11] and briefly recapitulated in [1]. This theory considers dynamic wetting as a particular case of a more general physical phenomenon, i.e. the fluid motion with formation/disappearance of interfaces. Since dynamic wetting is, by its very name, the process of creating a new — 'wetted' — solid surface, i.e. a fresh liquid-solid interface, it is clear that the surface properties of this interface, such as the surface tension, have to relax from some dynamic values at the contact line to their equilibrium values away from it. The surface-tension-relaxation process depends on the rate at which the bulk flow creates the free interface and, due to the resulting surface-tension gradient, has a reverse influence on the bulk flow. The *dynamic* surface tensions at the contact line 'negotiate' the appropriate value of θ_d to satisfy the (dynamic) Young equation, which represents the balance of forces acting on the contact line and replaces Eq. (5) one has in the slip models. The contact angle provides the boundary condition needed to determine the shape of the free surface and hence has a reverse influence on the bulk flow. As a result, the bulk flow, distributions of the surface tensions along the interfaces in the vicinity of the moving contact line and the value of the contact angle all become interdependent, and they all have to be found simultaneously as a solution to the corresponding mathematical problem. This problem is much more challenging mathematically than the one considered in the present paper and it will be addressed in a future work. The main question remains the same: is it possible to describe the data from [1] quantitatively with realistic values of the parameters involved? Preliminary estimates show that the key parameter determining the effect is the ratio of the length scale over which the surface tension relaxes to its equilibrium value and the length scale associated with the Stokes regime near the moving contact line. However, these qualitative conclusions are yet to be verified quantitatively.

It should also be mentioned that the experimental observations reported by Blake *et al.* [1] have recently been corroborated independently [26] using an improved apparatus. The key qualitative features that seem to have led to the observed dependence of the contact angle on the flow geometry are: (a) a relatively high wetting speed and (b) a sufficiently small length scale characterizing the variation of the flow field allowed by the curtain coating set-up. Recently, it has been shown experimentally [27] that in another flow configuration, namely that of an impacting drop, the observed contact angle also depends, besides the contact-line speed, on the flow field in the vicinity of the contact line. Together with the results of Refs. [1, 26] this suggests that the nonlocal hydrodynamic influence on the contact angle is a generic phenomenon and more research into it is required to investigate the effect of different fluid/solid combinations as well as various flow configurations.

APPENDIX A: COMPUTATIONAL DETAILS

The governing equations for the simulations presented here are the dimensionless Navier-Stokes equations appropriate for an isothermal incompressible Newtonian liquid of density ρ, viscosity μ, and surface tension σ experiencing a gravitational acceleration of g:

$$Re\boldsymbol{u}.\nabla\boldsymbol{u} \;=\; \nabla.\boldsymbol{T} + (Bo/Ca)\hat{\boldsymbol{g}}, \qquad (A1)$$
$$\nabla.\boldsymbol{u} \;=\; 0, \qquad (A2)$$

where $\boldsymbol{u} = (u, v)$ is velocity, $\hat{\boldsymbol{g}}$ is a unit vector indicating the direction of gravity, and $\boldsymbol{T}$ is the stress tensor with components $T_{\alpha\beta} = -p\delta_{\alpha\beta} + \partial u_\alpha/\partial x_\beta + \partial u_\beta/\partial x_\alpha$ (p being the pressure). The velocity is scaled by the substrate speed, U, while lengths are scaled by the coated film thickness, Q/U (where Q is the flow rate), and stresses are scaled by $\mu U^2/Q$. The Reynolds, capillary and Bond numbers are therefore given by $Re = \rho Q/\mu$, $Ca = \mu U/\sigma$, and $Bo = \rho g Q^2/\sigma U^2$ respectively. The numerical values of Re and Ca are given in Sec. V; the Bond number varies from 8.34×10^{-3} to 0.093.

We solved Eqs. (A1) and (A2) numerically using a Galerkin, weighted residual finite element formulation in which the domain is tessellated using Taylor-Hood triangular elements featuring six velocity nodes and three pressure nodes. Such elements satisfy the LBB stability condition [28] and, with the pressure interpolation one order lower than that of velocity, no 'locking' occurs [29]. The general approach is well-established in the field of coating flow simulation [30] so only a brief description is given here.

The algebraic finite element equations are derived in terms of a right-angled 'master' element, which has local coordinates (ξ, η) as shown in Fig. 7(a). Within this element the velocity and pressure are expressed in terms of their nodal values, $\boldsymbol{u}_i, p_j$, by means of biquadratic (Q_i) and bilinear (L_j) interpolation functions:

$$\boldsymbol{u}(\xi,\eta) = \sum_{i=1}^{6} \boldsymbol{u}_i Q_i(\xi,\eta); \quad p(\xi,\eta) = \sum_{j=1}^{3} p_j L_j(\xi,\eta).$$
$$(A3)$$

With reference to Fig. 7(a) it is easy to see that the three linear functions are given by

$$L_1 = 1 - \xi - \eta, \quad L_2 = \xi, \quad \text{and} \quad L_3 = \eta,$$

and that each function is equal to unity when evaluated at the vertex to which it belongs and zero at the other vertices. The six quadratic functions Q_i have the same
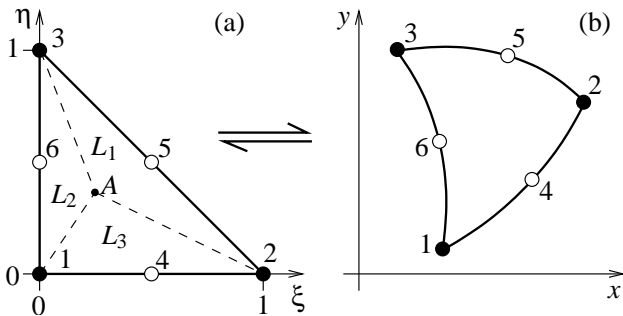
FIG. 7: (a) The 'master' element, with local coordinates (ξ, η), which is used to derive the finite element equations. The numbered black circles represent nodes at which velocity and pressure values are to be found, while the white circles are velocity-only nodes. The areas of the subtriangles formed by connecting point A to the vertices give, when divided by the total area of the element, the values of the linear interpolation functions L_j at point A. (b) A general element in physical space; the master element is mapped into each physical element by means of the quadratic transformation (A4).

property with respect to the six velocity nodes. The Q_i are also used to map the master element in local space into each general curved element in global $(x, y) = \boldsymbol{x}$ space (Fig. 7b) via the transformation

$$\boldsymbol{x}(\xi, \eta) = \sum_{i=1}^{6} \boldsymbol{x}_i Q_i(\xi, \eta), \tag{A4}$$

where $\boldsymbol{x}_i = (x_i, y_i)$ are the global coordinates of the element's nodes. The formulation of the weighted residual equations is completed by substituting Eqs. (A3) into Eqs. (A1) and (A2), weighting these by Q_i and L_j respectively, integrating over the entire domain, Ω, and requiring the resulting expressions to vanish. After some manipulation using vector identities and the divergence theorem, the equations to be solved become

$$\int_{\Omega} [Q_i Re \boldsymbol{u}.\nabla \boldsymbol{u} \;+\; \nabla Q_i.\boldsymbol{T} - Q_i(Bo/Ca)\hat{\boldsymbol{g}}] d\Omega$$
$$- \int_{\partial\Omega} Q_i \hat{\boldsymbol{n}}.\boldsymbol{T} ds = 0 \tag{A5}$$

and

$$\int_{\Omega} L_j \nabla.\boldsymbol{u} d\Omega = 0, \tag{A6}$$

where $d\Omega = dxdy$, $\hat{\boldsymbol{n}}$ is a unit normal to the boundary, $\partial\Omega$, of the domain, and s is arc length along the boundary.

The boundary conditions for the problem are as follows. On the (stationary) walls of the slot feeding the curtain (Fig. 1), the no-slip condition is applied. On the substrate being coated, either the Navier condition, Eq. (4), or an exponential velocity distribution, Eq. (2), is applied (see Sec. II) along with the impermeability condition $v = 0$. On the free surfaces we have the kinematic

condition,

$$\hat{\boldsymbol{n}}.\boldsymbol{u} = 0, \tag{A7}$$

together with (a) the condition of zero tangential stress (the viscosity of the ambient gas being negligible) and (b) the balance of normal stress with capillary pressure. Mathematically, conditions (a) and (b) are encapsulated in the form [31]

$$\hat{\boldsymbol{n}}.\boldsymbol{T} = \frac{1}{Ca}\frac{d\hat{\boldsymbol{t}}}{ds}, \tag{A8}$$

where $\hat{\boldsymbol{t}}$ is the unit tangent to the free surface. This can be inserted directly into Eq. (A5) and, after integrating by parts, the boundary integral becomes

$$\frac{Q_i}{Ca}[\hat{\boldsymbol{t}}_E - \hat{\boldsymbol{t}}_B] - \frac{1}{Ca}\int_{\partial\Omega_{FS}} \hat{\boldsymbol{t}}\frac{dQ_i}{ds}ds, \tag{A9}$$

where $\hat{\boldsymbol{t}}_B$ and $\hat{\boldsymbol{t}}_E$ are the unit tangents to the beginning and end of the free surface respectively, and $\partial\Omega_{FS}$ represents the free surface part of the domain boundary. The remaining boundary conditions are a parabolic velocity profile imposed at the top of the feed slot, a uniform velocity profile imposed where the film leaves the domain, and the condition that the upstream free surface meets the substrate at an angle equal to θ_d.

The free surface parametrization is based on the 'spine' approach developed by Kistler and Scriven [31, 32]. The essence of the method is that each node on a free surface is constrained to lie along one of a set of conveniently defined lines or curves (known as 'spines') which intersect the free surface. For example, a simple linear spine (numbered i, say) is defined by its base point, $\boldsymbol{b}_i$, which may be fixed or may lie on another spine, and its unit direction vector, $\hat{\boldsymbol{e}}_i$. The free-surface node lying on this spine is then located at $\boldsymbol{x} = \boldsymbol{b}_i + h_i\hat{\boldsymbol{e}}_i$, i.e. a distance h_i along the spine from its base point. Between the free-surface nodes the shape of the free surface is given via the curved edges of the elements which lie along the surface, i.e. by Eq. (A4). Hence the free surface is represented by a piecewise quadratic curve. Nodes in the interior of the domain are positioned along the spines according to some suitable (often uniform) distribution, e.g. $\boldsymbol{x}_j = \boldsymbol{b}_i + w_j h_i\hat{\boldsymbol{e}}_i$. The set of all h_i then forms a set of parameters which completely describes the free surfaces *and* allows the interior mesh to deform in response to deformations of the free surfaces. The unknown h_i are determined by forming a weighted residual from Eq. (A7), i.e. by solving

$$\int_{\partial\Omega_{FS}} Q_i \hat{\boldsymbol{n}}.\boldsymbol{u} ds = 0. \tag{A10}$$

In the mesh used here, linear spines are used to parametrize the falling curtain part of the free surfaces, but in order to achieve a convenient means of refining the mesh towards the contact line it was more appropriate to use circular spines in the 'heel' region of the domain. The
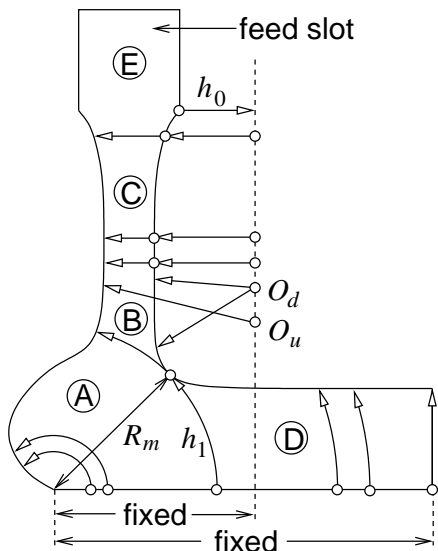
FIG. 8: The system of linear and circular spines used to parametrize the free surfaces. Spine base points are shown as circles. Regions A and D feature circular spines centered on the contact line; region B is represented in terms of linear spines based at two polar origins, O_u and O_d, with circular arcs constructed between the free surfaces; region C's spines are linear and horizontal; and region E is the feed slot, where the mesh is fixed.
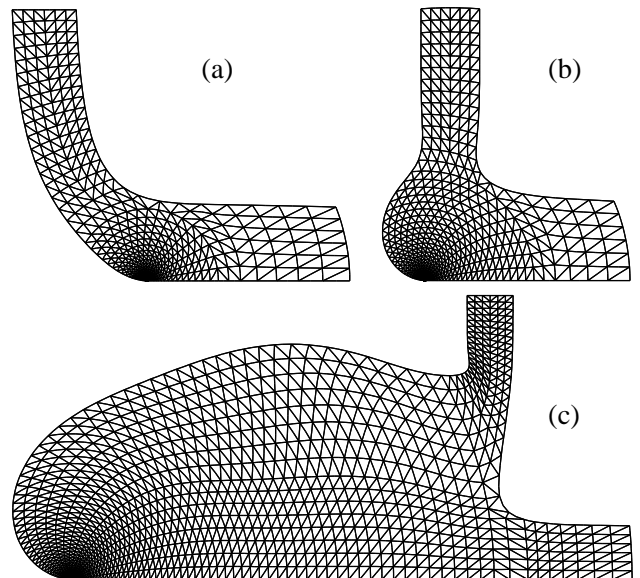

FIG. 9: Part of the computational mesh showing the node distribution for (a) the low flow rate limit, (b) a typical medium flow rate, and (c) the high flow rate limit. Note that the meshes are not shown on the same scale.
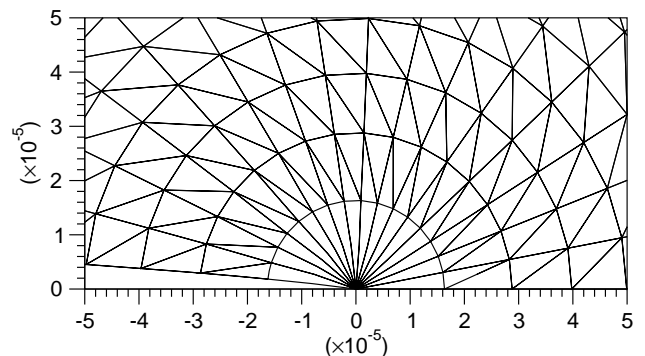

FIG. 10: A close-up view of the mesh near the contact line, formed by magnifying Fig. 9(b) by a factor of 10^5. The coordinates on the axes are in units of coating film thickness, which in this case is 428 μm.

complete spine system is illustrated in Fig. 8. The circular spines are defined by a centre point (in most cases the contact line), a radius, and a base point; the parameter h_i for these spines is then the angle subtended at the centre point by the base point and the relevant free surface node. The most important spine in Fig. 8 is h_0, which tethers the contact line (and indeed the entire free-surface mesh) to the fixed wall of the feed slot by defining the location of the vertical baseline shown in the diagram. The value of h_0 (i.e. the length of the spine) is determined from the condition that the upstream free-surface must meet the solid substrate at an angle of θ_d. Other important quantities upon which mesh regions A, B and D depend are the angle of the circular spine h_1 and the associated radial distance R_m which together locate the point on the downstream free surface which is closest to the contact line. The radii of the circular spines in regions A and D are given as fractions or multiples of R_m.

The spine system in Fig. 8 enabled the same mesh structure to be used under both low and high flow rate conditions, see Fig. 9. For high flow rates, additional strips of elements were simply inserted to maintain mesh quality. Close to the dynamic contact line, the density of the mesh was chosen so that the large velocity gradients on the solid surface were sufficiently well-represented. Hence the size of the elements in the slip region was at least an order of magnitude smaller than the slip length scale. Near the contact line the mesh must also be suitably fine in the aziumthal direction in order to capture

the velocity field with sufficient accuracy. A close-up of the mesh near the contact line is given in Fig. 10. The density of the rest of the mesh was adequate for further refinements to produce only negligible changes to the solution. As an illustration of the effect of mesh density, Fig. 6 includes (as black circles) the results from a repeat of the $\beta = 10$ kg cm^{-2} s^{-1} (curve 3) calculations made using meshes with approximately twice the node density of those used to generate curve 3. The results are indistinguishable on the scale of the graph.

In the slip models that we consider, the pressure becomes logarithmically singular as one approaches the contact line. For example, for Eq. (4), to leading order as the (dimensionless) distance r from the contact line goes

to zero, one has

$$p = \frac{\beta U}{\theta_d} \ln r + \dots, \qquad (A11)$$

whereas the stream function in local polar coordinates has the form $\psi = Ur^2 F(\theta)$, where

$$F(\theta) = B_1 + B_2\theta + B_3 \sin 2\theta + B_4 \cos 2\theta,$$

with

$$B_1 = -B_4 = -\frac{\beta l}{4\mu}, \quad B_2 = -\frac{1}{\theta_d}B_1, \quad B_3 = B_1 \cot(2\theta_d),$$

and this generates a regular flow field. (Here r is scaled as above by Q/U.) Since the pressure singularity in Eq. (A11) is integrable, it has been ignored in the computations reported in the literature, and the pressure over the elements comprising the contact line was approximated in the same way as in the bulk (described above). However, the computational mesh necessarily includes a pressure node located at the contact line. Since the solution cannot return the correct (i.e. negatively infinite) value of pressure at this node, it is desirable to redefine the pressure interpolation on the elements touching the contact line so as to avoid having a finite pressure at this point and hence to obtain a uniformly valid solution.

Following Suckling [33], to cope with the singular pressure field at the contact line, the linear pressure interpolation functions in the elements adjacent to the contact line were augmented with logarithmic functions corresponding to Eq. (A11). Consider Fig. 7(a) in the context of an element adjacent to the contact line. The numbering system employed in the computational mesh is chosen so that local node 1 corresponds to the contact line. Using Eq. (A4), we therefore have

$$r(\xi,\eta) = |\boldsymbol{x} - \boldsymbol{x}_1| = \left[\left(\sum_{i=1}^{6}\{x_i Q_i(\xi,\eta)\} - x_1 \right)^2 \right.$$
$$\left. - \left(\sum_{i=1}^{6}\{y_i Q_i(\xi,\eta)\} - y_1 \right)^2 \right]^{1/2} (A12)$$

and the logarithmic singularity can be incorporated by replacing interpolation function L_1 by

$$L_1^* = L_1 \ln r = (1 - \xi - \eta) \ln r. \qquad (A13)$$

The pressure is then given by

$$p(\xi,\eta) = p_1 L_1^* + p_2 L_2 + p_3 L_3.$$

Note that L_1^* vanishes along the element edge opposite the contact line (between nodes 2 and 3), and therefore the augmented elements are completely compatible with the regular elements used in the bulk of the domain. As node 1 is approached, i.e. as $\xi,\eta \to 0$ and hence $r \to 0$, however, L_1^* provides the correct functional form
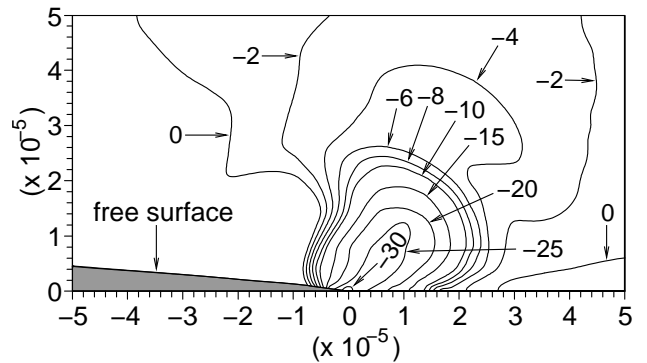

FIG. 11: Typical dimensionless pressure contours in the vicinity of the dynamic contact line. The field of view covers the same area as Fig. 10. In this case $Q = 3 \text{ cm}^2\,\text{s}^{-1}$ and $\theta_d = 169°$. Note that the contour labels show multiples of 1000.

to match Eq. (A11). Importantly, using this approach, p_1 no longer represents a finite (and therefore incorrect) value of pressure at the contact line, but instead provides the coefficient multiplying $\ln r$.

The integration of the residual equations (A5), (A6) and (A10) is achieved on an element-by-element basis using the master element and transformation (A4), and the pressure gradient terms in the Navier-Stokes equations give rise to integrals over the master element of the form

$$\iint p_j L_j(\xi,\eta) \left(\frac{\partial Q_i}{\partial \xi}\frac{\partial y}{\partial \eta} - \frac{\partial Q_i}{\partial \eta}\frac{\partial y}{\partial \xi} \right) d\xi d\eta \qquad (A14)$$

and

$$\iint p_j L_j(\xi,\eta) \left(\frac{\partial Q_i}{\partial \eta}\frac{\partial x}{\partial \xi} - \frac{\partial Q_i}{\partial \xi}\frac{\partial x}{\partial \eta} \right) d\xi d\eta, \qquad (A15)$$

where $\partial y/\partial \eta$ etc. are found from Eq. (A4). Away from the contact line, the integrands are polynomials in ξ and η (as are those arising from the other terms in the Navier-Stokes equations) and the integration of all terms is performed numerically by means of Gaussian quadrature. However, insertion of Eq. (A13) into integrals (A14) and (A15) — and indeed the continuity equation, where it also appears — produces integrands which are not regular polynomials, and therefore standard Gaussian quadrature is not appropriate for calculating these integrals. Another issue is that Eq. (A13) of course cannot be evaluated at the contact line itself. To enable the calculation of these integrals, a small region of radius ϵ around node 1 is excluded from the master element, and a recursive adaptive Simpson's rule quadrature is used to integrate over the remainder of the element. Suckling [33] showed that the error in excluding the contact line region is $O(\epsilon^2 \ln \epsilon)$ as $\epsilon \to 0$, and tested the quadrature procedure against similar integrals for which exact solutions are known. We tested our implementation of the method in the same way, and used the value $\epsilon = 10^{-12}$ in gener-

ating the results presented in this paper. A plot of the pressure field close to the contact line is given in Fig. 11.

Note that the singularity in the pressure field also gives rise to a corresponding integrable singularity in the free-surface curvature at the contact line, though the contact angle remains well-defined. Unlike the pressure field, however, the singularity in curvature does not require any special treatment since the normal and tangential stress conditions are imposed in integral form, see Eq. (A8), and therefore the only requirement for a uniformly convergent

solution is that the curvature should be integrable, which it is. The fact that the free-surface discretization is sufficient is demonstrated by the mesh-independence of the results (see Fig. 6).

Finally, the residual equations were solved using Newton iteration in which the Jacobian at each iteration was inverted by the frontal method [34]. The iterative process was terminated when the L_2 norm of the residuals fell below 10^{-8}; typically 4–8 iterations were needed to satisfy this criterion.

[1] T. D. Blake, M. Bracke, and Y. D. Shikhmurzaev, Phys. Fluids **11**, 1995 (1999).

[2] T. D. Blake, A. Clarke, and K. J. Ruschak, AIChE J. **40**, 229 (1994).

[3] R. J. Hansen and T. Y. Toong, J. Colloid Interf. Sci. **36**, 410 (1971).

[4] Y. D. Shikhmurzaev, J. Fluid Mech. **334**, 211 (1997).

[5] M. Y. Zhou and P. Sheng, Phys. Rev. Lett. **64**, 882 (1990).

[6] P. Sheng and M. Zhou, Phys. Rev. A **45**, 5694 (1992).

[7] D. E. Finlow, P. R. Kota, and A. Bose, Phys. Fluids **8**, 302 (1996).

[8] E. B. Dussan V., J. Fluid Mech. **77**, 665 (1976).

[9] M. Navier, Mem. Acad. Sci. Inst. Fr. pp. 389–440 (1823).

[10] H. Lamb, *Hydrodynamics* (Dover, New York, 1932).

[11] Y. D. Shikhmurzaev, Int. J. Multiphase Flow **19**, 589 (1993).

[12] R. A. Hayes and J. Ralston, J. Colloid Interf. Sci. **159**, 429 (1993).

[13] R. L. Hoffman, J. Colloid Interf. Sci. **50**, 228 (1975).

[14] C. G. Ngan and E. B. Dussan V., J. Fluid Mech. **118**, 27 (1982).

[15] P. Bach and O. Hassager, J. Fluid Mech. **152**, 173 (1985).

[16] R. G. Cox, J. Fluid Mech. **168**, 169 (1986).

[17] M. Fermigier and P. Jenffer, J. Colloid Interf. Sci. **146**, 226 (1991).

[18] L. M. Hocking and A. D. Rivers, J. Fluid Mech. **121**, 425 (1982).

[19] C. Huh and S. G. Mason, J. Fluid Mech. **81**, 401 (1977).

[20] L. M. Hocking, J. Fluid Mech. **79**, 209 (1977).

[21] L. M. Hocking, Q. J. Mech. App. Math. **34**, 37 (1981).

[22] L. M. Hocking, J. Fluid Mech. **239**, 671 (1992).

[23] P. A. Durbin, J. Fluid Mech. **197**, 157 (1988).

[24] V. V. Pukhnachev and V. A. Solonnikov, PMM — App. Math. & Mech. **46**, 961 (1982).

[25] C. Baiocchi and V. V. Pukhnachev, J. Appl. Mech. Techn. Phys. (USSR) pp. 27–40 (1990).

[26] A. Clarke and E. Stattersfield, Phys. Fluids, submitted (2006).

[27] Š. Šikalo, H.-D. Wilhelm, I. V. Roisman, S. Jakirlić, and C. Tropea, Phys. Fluids **17**, 062103 (2005).

[28] I. Babuska and A. K. Aziz, in *Mathematical Foundations of the Finite Element Method with Applications to Partial Differential Equations*, edited by A. K. Aziz (Academic Press, New York, 1972), pp. 1–135.

[29] T. J. R. Hughes, *The Finite Element Method: Linear Static and Dynamic Finite Element Analysis* (Prentice-Hall, 1987).

[30] S. F. Kistler and P. M. Schweizer, *Liquid Film Coating: scientific principles and their technological implications* (Chapman and Hall, 1997).

[31] S. F. Kistler and L. E. Scriven, in *Computational Analysis of Polymer Processing*, edited by J. R. A. Pearson and S. M. Richardson (London & New York: Applied Science, 1983), pp. 243–299.

[32] S. F. Kistler and L. E. Scriven, Int. J. Num. Meth. Fluids **4**, 207 (1984).

[33] P. M. Suckling, Ph.D. thesis, University of Birmingham (2003).

[34] P. Hood, Int. J. Num. Meth. Eng. **10**, 379 (1976).